Surface modification of BaTiO₃ with catechol surfactant and effects on cold sintering

Cite as: J. Appl. Phys. 129, 184102 (2021); https://doi.org/10.1063/5.0049905 Submitted: 10 March 2021 • Accepted: 19 April 2021 • Published Online: 10 May 2021

🗓 Takao Sada, 🗓 Arnaud Ndayishimiye, Zhongming Fan, et al.

COLLECTIONS

Paper published as part of the special topic on Control of Functionality at Interfaces







ARTICLES YOU MAY BE INTERESTED IN

Enhanced high permittivity BaTiO₃-polymer nanocomposites from the cold sintering process Journal of Applied Physics 128, 084103 (2020); https://doi.org/10.1063/5.0021040

BaTiO₃-based piezoelectrics: Fundamentals, current status, and perspectives Applied Physics Reviews 4, 041305 (2017); https://doi.org/10.1063/1.4990046

Cold sintering of yttria-stabilized cubic bismuth oxide: Conductivity and microstructural evolution of metastable grain boundaries with annealing

Journal of Applied Physics 128, 215104 (2020); https://doi.org/10.1063/5.0014287



Journal of Applied Physics Special Topics Open for Submissions

Surface modification of BaTiO₃ with catechol surfactant and effects on cold sintering

Cite as: J. Appl. Phys. 129, 184102 (2021); doi: 10.1063/5.0049905

Submitted: 10 March 2021 · Accepted: 19 April 2021 ·

Published Online: 10 May 2021









Takao Sada,^{1,2,3} 📵 Arnaud Ndayishimiye,^{2,3} 📵 Zhongming Fan,^{2,3} Yoshihiro Fujioka, ¹ and Clive A. Randall^{2,3,a)} 📵



AFFILIATIONS

- Monozukuri R&D Laboratory, KYOCERA Corporation, Kirishima, Kagoshima 899-4312, Japan
- ²Materials Research Institute, The Pennsylvania State University, University Park, Pennsylvania 16802, USA
- ³Department of Materials Science & Engineering, The Pennsylvania State University, University Park, Pennsylvania 16802, USA

Note: This paper is part of the Special Topic on Control of Functionality at Interfaces.

^{a)}Author to whom correspondence should be addressed: car4@psu.edu

ABSTRACT

The sintering of functionalized particles is an approach often used to obtain high performance functional ceramics. When molecular surfactants are used to functionalize particles, conventional sintering cannot be applied due to extremely high processing temperatures. Here, BaTiO₃ particles are grafted with different coverages using a catechol (CA) surfactant, and then these particles are densified under cold sintering with a (BaOH₂)·8H₂O transient flux. The adsorption of CA is equilibrated with various concentrations on BaTiO₃ particles at room temperature. The modeling (Langmuir and Freundlich adsorption) and the quantification (UV-vis absorption and thermogravimetric analysis) of CA coverage enable us to rigorously determine the degree of functionalization and conduct thorough cold sintering kinetics investigations as a function of CA coverage using a dilatometer. Microstructure is observed with electron microscopy techniques to determine the grain and grain boundary interfaces that result with the competition of surfactant coverage and densification driven by the dissolution and reprecipitation processes at the interfaces. A mechanism with the retardation of cold sintering kinetics is discussed based on these experimental observations.

Published under an exclusive license by AIP Publishing. https://doi.org/10.1063/5.0049905

I. INTRODUCTION

Cold sintering is a new sintering method that enables the densification of materials at low temperatures. Typical conventional sintering temperatures (T_s) relative to the material's melting temperature ($T_{\rm m}$) are between $0.5 < T_{\rm s}/T_{\rm m} < 0.95$. With cold sintering, this temperature is vastly reduced, near $T_s/T_m < 0.2$. Cold sintering requires the use of a transient fluid phase, chemically active to enable a chemo-mechanical mechanism, inducing dissolution, transport, and precipitation. These steps are kinetically aided with the application of moderate uniaxial stresses and temperatures. The transient fluid phase can be introduced in the ceramic powders as a pure liquid solvent, a solution (acidic or basic), a suspension (liquid solvent mixed with chelating agents or hydrous acetates, among others), or solid hydroxides (hydrated or non-hydrated) that melt during the process. As recently discussed, there are several chemical pathways that can drive the cold sintering process.⁵ During the stress-induced dissolution at grain contacts, it is important for the solid to be sintered to have a high solubility in the selected transient fluid phase, and preferably congruent dissolution. The coupled processes that underpin cold sintering are closely related to a mechanism known as pressure solution creep that enables the compaction and porosity reduction in sedimentary rock.6

The theoretical underpinning of pressure solution creep links to back to local differences in chemical potentials, μ at the interface at the particle contact and at the pore surfaces. These gradients in chemical potential drive a solute diffusion to the pores between the particles. Figure 1 shows a basic schematic of the pressure solution creep mechanism that permits densification in cold sintering. The dissolution, transport, and precipitation are all connected, and each can be a rate-limited step to sintering. The kinetics of dissolution can be influenced by the: (i) the nature of chemistry at the contact solid-liquid-solid interface, (ii) particle size distribution, (iii) applied stress and its associated local stress, and (iv) temperature activating diffusion and surface reaction kinetics.

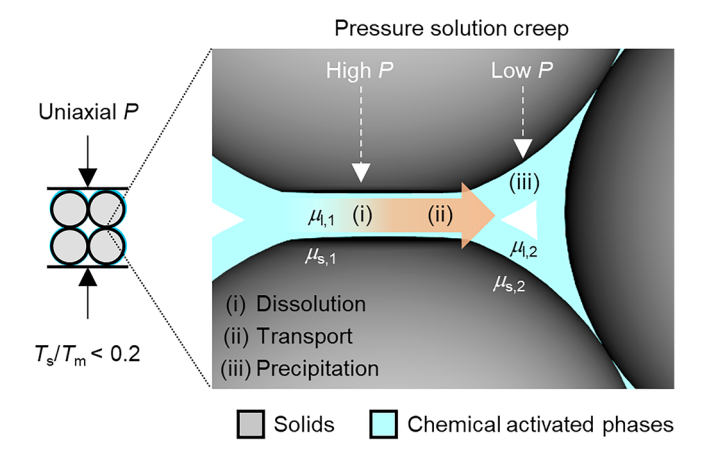


FIG. 1. Schematic illustration of the pressure solution creep. The local differences in chemical potentials (μ) between solid $(\mu_{s,1})$ /liquid $(\mu_{l,1})$ and liquids with different concentrations of dissolved species $(\mu_{l,1}$ and $\mu_{l,2})$, and liquid $(\mu_{l,2})$ /solid $(\mu_{s,2})$, drives (i) dissolution, (ii) mass transport, and (iii) precipitation, leading to cold sintering densification.

In this study, we introduce an additional factor that can potentially compete with the dissolution and/or precipitation, and this is the mediation of the surface activity with the use of a surfactant.

Typically, in the sintering of ceramics, the temperatures are extremely high, and, therefore, the molecular surfactants on the particulates are irrelevant to each other, even though both phenomena are thermodynamically driven in the minimization of surface free energy. 10-13 With the low temperatures used in cold sintering, the surface modifications that are typically considered with colloidal chemistry can now be connected. Surfactants are small amphiphilic molecules that lower the surface energy in a colloidal system. Surfactants aid dispersion and undergo adsorption to surfaces, and this modifies the chemical potential and the surface energy as formulated under the Gibbs-Langmuir and/or the Freundlich adsorption isothermal models. 14-17 The coverage of a particle surface under isothermal adsorption is impacted by the concentration of surfactants in the liquid and thereby provides a means for controlled surface functionalization, and then considers the impact on densification.

Earlier, there have been investigations on the influence of surfactants on the Ostwald ripening kinetics of nanoparticles. During Ostwald ripening, small particles or dissolved species precipitate onto larger particles, leading to their coarsening, driven by chemical potential differences. Surfactant adsorption is used in nanoparticle synthesis to aid dispersion and to narrow or focus the particle size distribution following an Ostwald ripening mechanism. The surfactant coverage and chain lengths influence the kinetics of the growth rate, and this depends on the surfactant type and the surfactant coverage. So, we anticipate that surfactants will likewise have a perturbing influence on the densification mechanism under cold sintering. ^{18–20}

In this paper, we introduce a controlled approach to functionalize BaTiO₃ particles with catechol molecules and then investigate their effects on cold sintered dielectrics with respect

to densification, densification kinetics, microstructures, and associated electrical properties.

II. EXPERIMENTAL

A. Material supplies

The basic $BaTiO_3$ powders (average particle size: 100 nm) synthesized with the typical oxalate method were supplied by Kyocera (Kagoshima, Japan). The cold sintering transient phase was selected to be barium hydroxide octahydrate (> 98%), and this was purchased from Alfa Aesar and used as received. The surfactant that was used was catechol (CA > 99%) and was purchased from Sigma Aldrich.

B. Surface modification

1. CA treatment

The as-received BaTiO₃ powder was first calcined at 700 °C for 60 min to completely remove organic residues that can age a powder and impact the nature of the particle surface. Powders after this treatment were stored in a vial with a parafilm sealing film to minimize future aging from atmospheric conditions, especially humidity effects that accelerate oxycarbonates.²¹ The surfactant solution was prepared with different amounts of CA (0.25, 0.5, 1.0, 2.0, and 4.0 mg) dissolved in 10 ml of ethanol. Then, 1.0 g of the pre-heat treated BaTiO₃ powder (BET surface area = $9.85 \text{ m}^2 \text{ g}^{-1}$) was added to the CA ethanol solutions. The mixtures were stirred at room temperature for 30 min. The treated powder and the supernatant were separated by centrifugation. The precipitate was washed with an excess amount of ethanol, followed by centrifugation to remove the unreacted surfactant. The washing process was repeated twice. After washing, the surface-modified particles were then dried in a vacuum oven at 80 °C for 24 h.

2. Evaluation of CA-treated BaTiO₃

To quantify surface coverage, a thermogravimetric analysis (TGA) was conducted on pre-heat treated BaTiO₃ and CA-treated BaTiO₃, using SDT Q600 (TA Instrument) at a heating rate of 10 °C min⁻¹ under a 100 ml min⁻¹ air flow. The amount of CA in the CA-treated BaTiO₃ was estimated by the mass difference between pre-heat treated BaTiO₃ and CA-treated BaTiO₃ in the temperature range between 180 and 410 °C. Additional analysis of the CA coverage was performed with a spectroscopic UV-vis method and using the KM function (Lambda 950 UV-Vis Spectrophotometer, Perkin-Elmer). Fourier transformed infrared spectroscopy (FTIR) experiments were conducted using a Bruker Vertex 70 FTIR spectrometer (Billerica) with an attenuated total reflection (ATR) accessory, equipped with a liquid nitrogen-cooled MCT detector. Spectra were collected at room temperature and were obtained from an average of 200 scans in the wavelength range of 500–4000 cm⁻¹.

C. Cold sintering

1. Cold sintering of $BaTiO_3$ with different surface coverages

 $0.75\,\mathrm{g}$ of CA-treated BaTiO₃ and $0.12\,\mathrm{g}$ of Ba(OH)₂·8H₂O solid powders were homogeneously ground and mixed using a

pestle and mortar before sintering. For the untreated sample, the pre-heat treated BaTiO₃ was used. The mixture was loaded into a 12.7 mm diameter die and uniaxially pressed under 350 MPa. Since the melting point of Ba(OH)₂·8H₂O is 78 °C, a pre-heating step was conducted at 80 °C for 30 min to allow its homogeneous distribution in the starting powder. Then, the set temperature was increased to 200 °C using both a heater jacket and a press equipped with hot plates and held for 75 min under 350 MPa. The pressure was applied before ramping up and released immediately after the dwell time. Samples were cooled down to room temperature. The as-prepared samples after cold sintering were dried and stored in an oven at 200 °C.

2. Densification-in situ dilatometry

Prior to sintering, the powder mixture [0.75 g of CA-treated BaTiO₃ and 0.12 g of Ba(OH)₂·8H₂O] was compacted at room temperature, under 350 MPa for 10 min. The data collected during sintering (using a 10 °C/min average heating rate, a temperature of 200 °C, a dwell time of 75 min, under 350 MPa) were then corrected with the thermal behavior of the empty die in analogous conditions. The obtained time-dependent shrinkage information s(t) was converted into relative density $d_{rel}(t)$, using the following equation:

$$d_{rel}(t) = \frac{m_f}{\pi \times r_f^2 \times (t_f + |s(t)|) \times \rho_{theo}},$$
 (1)

where m_f , r_f , and t_f are, respectively, the mass, the radius, and the thickness of the final pellet. The *in situ* densification was performed on a modified dilatometer first described by Floyd *et al.*, which permits accelerate shrinkage and thermal measurements of cold sintering, under controlled temperature profiles and isobaric pressure conditions.²² The dilatometer apparatus that was used in this study is shown in Fig. S1 of the supplementary material.

3. Evaluation of cold sintered BaTiO₃

Bulk densities (ρ_b) were obtained by the Archimedes' method, performed using ethanol. Theoretical densities (ρ_{th}) were considered for pure BaTiO₃ (6.03 g cm⁻¹). The relative density was then calculated from the ρ_b/ρ_{th} ratio. Scanning electron microscopy (SEM) images of microstructure with sputtered iridium were observed using the fracture surface of the samples at an accelerating voltage of 5 kV (Apreo SEM, Thermo Scientific). For the grain size measurement, the major axis of at least 200 grains was counted using SEM images of the fractured surface. For the electrical property measurements, 100 nm-thick Ag electrodes were deposited by sputtering (Q150R Plus, Quorum Technologies) on polished surfaces. Dielectric properties were measured at 1 MHz in the temperature range between 10 and 200 °C, using an LCR meter (E4980A, Agilent Technologies). The resistivity was measured using a HP 4140B pA meter with a Trek Model 610D high voltage amplifier system at room temperature. Transmission electron microscopy (TEM) for high-resolution microstructure analysis was measured at 200 kV (TALOS F200X, FEI, USA), while the TEM specimen was prepared using a focused ion beam (FIB) system (Helios 660, FEI).

III. RESULTS AND DISCUSSION

The simple structure of catechol (CA), also known as a benzenediol organic compound with a molecular formula $C_6H_4(OH)_2$, is shown in Fig. 1(a). CA has been considered a surfactant in many different oxide particle surfaces but mainly on anatase and rutile TiO₂ nanoparticles.^{23–28} When used as a surfactant with BaTiO₃, there is a color change, indicating an interfacial charge transfer (ICT) on the adsorption of the CA molecule.²⁹ Indeed, the change in color from white to light yellow is observed immediately after the mixing of CA with BaTiO₃, as shown in Fig. 2(a), indicating the formation of their complexes through chemisorption. As shown in SEM images of the powders (Fig. S2), no obvious changes in microstructures and size of the nanoparticles are observed after the treatment. Fujisawa et al. conducted a detailed spectroscopy and density functional theory (DFT) investigation and concluded that CA chemisorption on a BaTiO₃ surface was taking place by a bridge coordination with two adjacent Ti atoms and chelate coordination with a single Ti atom, respectively [Fig. 2(b)].³⁰ It was noted that typically, we expect a partitioning of the complexing with 30% bridging and 70% chelating bonds.³⁰ The amount of catechol on BaTiO₃ was investigated using TGA and UV-vis absorption. While the bare BaTiO₃ shows the constant gradual mass loss with the temperature, an additional mass loss contribution is observed at approximatively 280 °C with increasing amount of CA [Fig. 2(c)]. A similar tendency was observed in the UV-vis diffusion reflectance spectra and modeled the absorption with the Kubelka-Munk function (K-M), where the absorbance of powders in the visible region increases with the amount of CA (Fig. S3). To evaluate the adsorption behavior, the mass loss at 410 °C obtained by TGA was replotted with respect to the amount of CA in Fig. 2(d). A steep increase at low concentrations and saturation at relatively high concentrations is confirmed. The systematic changes indicate that BaTiO₃ powders with different surface coverages were successfully fabricated. The presence of CA on our starting powders was investigated by FTIR spectroscopy (Fig. S4).

The CA adsorption is considered with respect to the Langmuir adsorption [Fig. 3(a)] and the empirical Freundlich adsorption [Fig. 3(b)] isothermal models. Since it is reported that the absorption of the complex (TiO₂-CA) in the visible region is correlated with the geometry of the attached CA, ²⁴ the amount of CA calculated from the TGA mass loss was adopted for this study. First, the Langmuir adsorption model considers at a maximum coverage, there is only a monolayer of surfactants on the surface, and these are attached to individual sites and each binding energy is similar at each site; there are no interactions between molecular adsorptions at neighboring sites. The Langmuir adsorption isotherm is given by

$$\frac{m}{m_{\infty}} = \frac{Kc}{(1+Kc)},\tag{2}$$

where m is the amount of surfactant CA (mg) adsorbed per unit mass of solids, m_{∞} is the amount required for the monolayer coverage, c is the equilibrium concentration in the solution, and K is the equilibrium constant. The Langmuir isotherm can be readily tested by rearranging into a linear form,

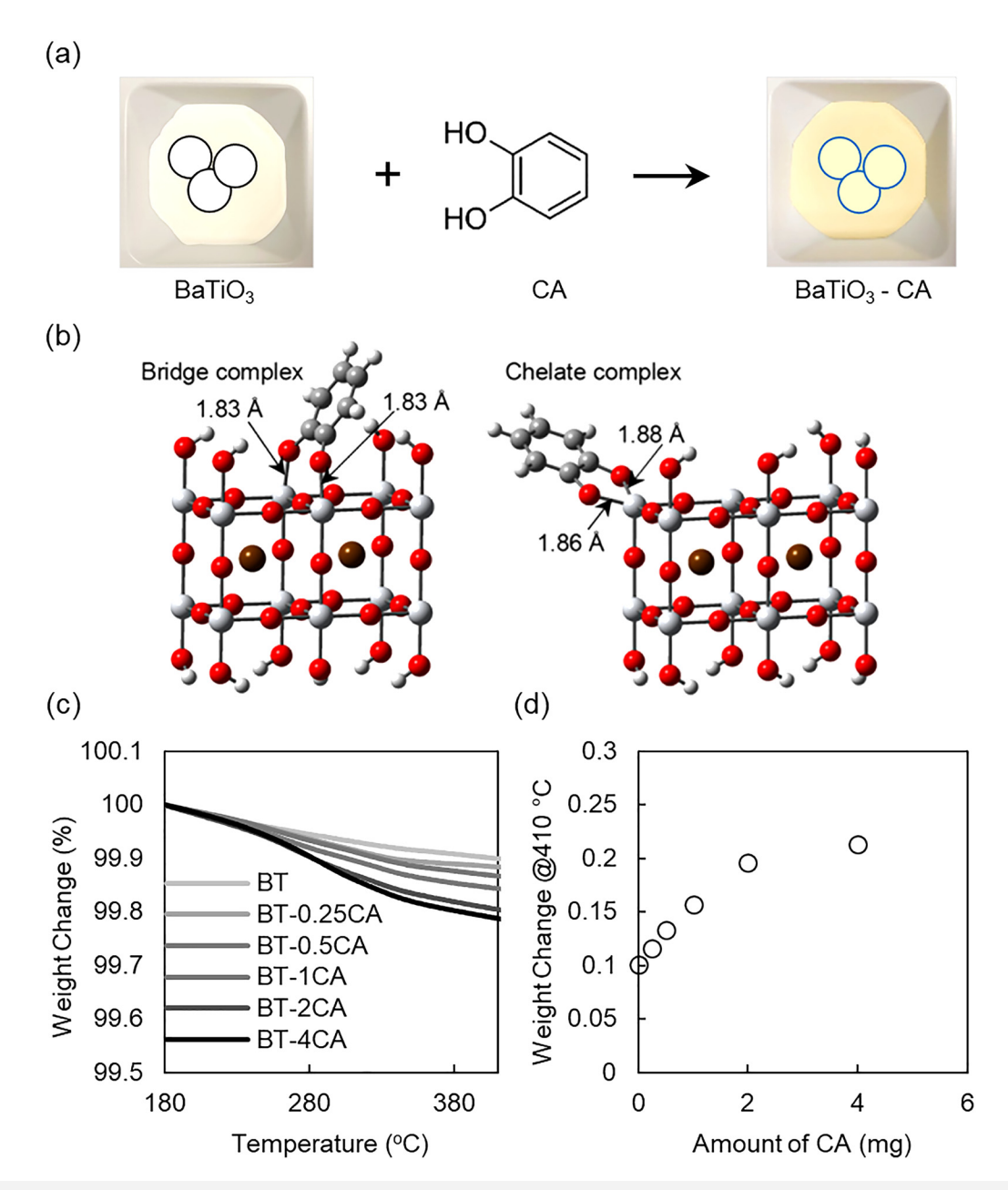


FIG. 2. (a) Schematic representation of BaTiO₃ powders before and after mixing with catechol (CA). (b) Bridge complex and chelate complex on BaTiO₃ surfaces as determined by DFT, with colors corresponding to each atomic species indicated as gray: carbon, small white: hydrogen, red: oxygen, large white: titanium, and brown: barium. Reproduced with permission from Fujisawa *et al.*, J. Phys. Chem. C **120**, 21162 (2016). Copyright 2016 American Chemical Society. (c) TGA curves of the BaTiO₃ powders with different CA coverages. 0, 0.25, 0.5, 1.0, 2.0, and 4.0 mg of CA were mixed with BaTiO₃ powders and named as BT, BT-0.25CA, BT-0.5CA, BT-1CA, BT-2CA, and BT-4CA, respectively. (d) Change in the mass loss at 410 °C as a function of CA amount.

$$\frac{1}{m} = \frac{1}{Km_{\infty}} \times \frac{1}{c} + \frac{1}{m_{\infty}}.$$
 (3)

Based on the intercept being $\frac{1}{m_{\infty}}$ with 0.49, m_{∞} (coverage) is estimated to be $m_{\infty} = 2.02 \pm 1.05$, and the slope is 0.001; therefore,

K is determined to be 494 ± 258 M. The grafting density of CA on the BaTiO₃ surface (BET surface area = 9.85 m² g⁻¹) is estimated to be $\theta_{\infty} = 1.12 \pm 0.63$ nm⁻². K and θ_{∞} are relatively lower than in rutile and anatase TiO₂, as shown in Table I. This could be due to the nature of the bonding, such as the CA dominance of the

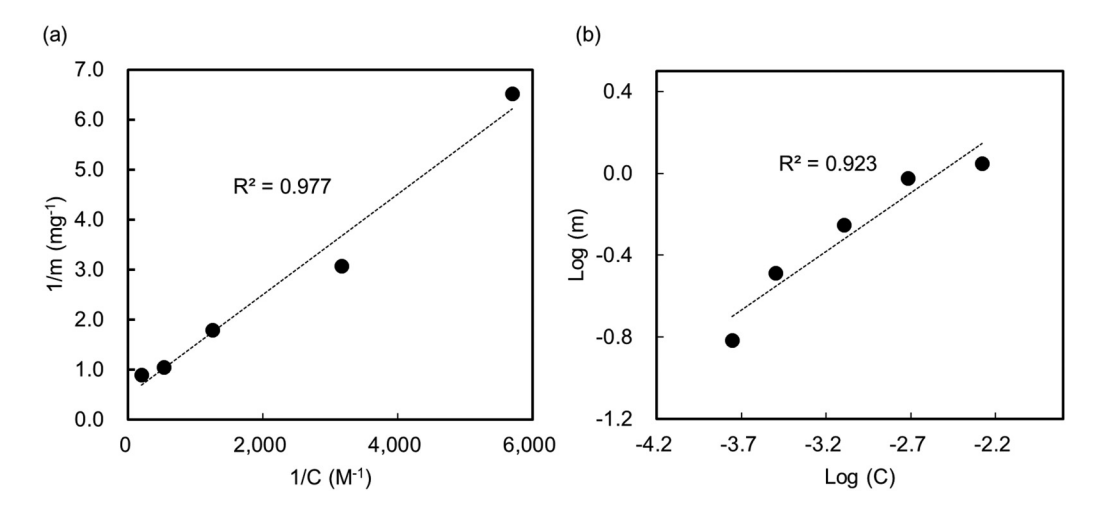


FIG. 3. (a) Langmuir and (b) Freundlich adsorption isotherm model for catechol (CA) on BaTiO₃. The amount of CA is estimated from the TGA mass loss. The fits were (a) R² = 0.977 and (b) 0.923.

chelate bonds to the BaTiO $_3$ surface. The chelate coordination is explained by the Ti–Ti interatomic distance, that is, ~4.01 Å, which is a significant 32% longer than that in TiO $_2$ and 52% longer than the distance between the oxygen interatomic distance in the CA molecule, which destabilizes the bridge coordination. Furthermore, as determined by the DFT calculations of Fujisawa et al, with the CA chemisorbs on a Ba-terminated surface of BaTiO $_3$, doing so weakens the Ti–O_{bridge} bonds significantly, and one of the Ti–O_{bridge} bonds is cleaved. All these first principles calculations of the chemisorb bonding predictions are consistent with our experimental observations of lower K and θ_∞ , as extracted with fitting to the Langmuir adsorption isotherm model.

For completeness, we also analyzed the experimental data with the Freundlich adsorption isotherm model. Here, there are no assumptions about the limits of a monolayer coverage, and this permits the binding energy to vary continuously from site to site on the solid surface. This allows variables that themselves may not be linearly related to be accessed. This is not the case here, given the success of the data plotted in Fig. 3(b). The empirical Freundlich expression is given by

$$\frac{n}{n_{\infty}} = kc^{1/\nu}.$$
(4)

This is plotted as $\log m$ against $\log c$, and we use the slope to evaluate v, which typically ranges between 1.5 and 3, as shown in Fig. 3(b), and v=1.7. The fact that the R² fitting is superior with the Langmuir model, and it rationalizes well with the first principles chemisorbed modeling, which points to the fact that CA is a monolayer coverage with a relative low grafting density, that is, impacted by the nature of the Ti bonds to the CA being perturbed with the Ba ions in the perovskite structure. The above quantification is used to systematically assess the CA coverage, and this then becomes the dependent variable in the following densification study.

A. Densification and microstructural evolution as a function of coverage

It is long-range forces that are common to surface behavior and fundamentally underpin the surface tension in both the surfactant adsorption and sintering phenomena, and control the surface energy. 32,33 In general, the thermodynamics of sintering is based upon Gibbs free energy (ΔG) minimization principles, occurring when a powder compact is transformed into a dense monolithic strong polycrystalline structure. 34 This is expressed with the following equation:

$$\Delta G = \gamma dA + A d\gamma, \tag{5}$$

TABLE I. Summary of K and θ_{∞} for oxides (TiO₂ and BaTiO₃) and catecholate ligands. The references are listed in the last column. STM, TGA, and UV–vis in the method are abbreviations for scanning tunneling microscope, thermogravimetric analysis, and ultraviolet–visible absorption spectroscopy, respectively.

Compound	Surfactant	Crystal structure	$K(M^{-1})$	$\theta_{\infty} (\mathrm{nm}^{-2})$	Method	Reference
TiO_2	Catechol	Rutile		~2	STM	24
TiO_2	4-tert-Butylcatechol	Anatase	679 ± 27	4.48 ± 0.18	Langmuir model TGA	15
TiO_2	Catechol	Anatase	8200	0.75	Langmuir model UV-vis	27
TiO_2	Catechol	Anatase	3820 ± 440		Benesi-Hildebrand UV-vis	28
BaTiO ₃	Catechol	Perovskite	494 ± 258	1.12 ± 0.63	Langmuir model TGA	This work

where γ is the surface energy of the particles, A is the surface area of the particles, and γdA is the term corresponding to reducing the surface area by coarsening processes such as the aforementioned Oswald ripening or through a coalescence of grains. $Ad\gamma$ is the term corresponding to changes in surface energies, such as creating new low energy surfaces, e.g., solid–solid interfaces, such as grain boundaries, and reducing higher energy solid–air surfaces. In general, both coarsening and formation of solid–solid interfaces are active in the sintering process and compete to the point where the coarsening can limit the overall final densification of a sintering material.

The thermodynamic driving force in cold sintering is enabled through an interface-driven mechanism known as pressure solution ⁹ The presence of a transient phase along with an applied stress led to the dissolution of solids at grain contacts, the diffusion through grain boundaries, and the precipitation at pore walls. 35,36 As shown in Fig. 1, these three steps of pressure solution creeps are induced by the existence of chemical potential differences between the solid stressed at grain contacts and the solid at pore surfaces. Earlier work in our group highlighted anisothermal heating rate studies, isothermal grain growth studies, and using tracers (isotopes and solid solution additives) to determine the epitaxial reprecipitation on grain surfaces to establish evidence through the formation of a core-shell.^{37–39} The energetics of the processes have been determined to be significantly lower than the equivalent activation energies under the cold sintering process relative to the conventional sintering process. There are no methods to experimentally and thoroughly investigate chemical reactions at interfaces in cold sintering process (CSP) conditions, nor in molten hydroxides. However, promising developments to monitor in situ changes in materials during CSP have been highlighted by Allen et al., using small angle scattering techniques. ReaxFF molecular dynamics simulations have pointed to complex and dynamic oxide/solvent chemical reactions that drive diffusion rates by orders of magnitude in grain boundaries.⁴¹ Recent investigations highlighted chemical reactions dynamics in the BT/NaOH-KOH system. 42 Although there might be several mechanistic similarities, a thorough discussion of chemical reactions in the BT/Ba(OH)2·8H2O system is beyond the scope of this paper.

Here, we consider the impact of adsorbed surfactants on the densification, kinetics, and mechanisms of cold sintering. The grafting density of BaTiO₃ with 0.25CA, 0.5CA, 1CA, 2CA, and 4CA is estimated to be 0.09, 0.18, 0.31, 0.52, and 0.62 (nm⁻²), respectively, based on the TGA results. The relative density of the cold sintered samples decreases gradually with an increase in the grafting density after the dwell time of 75 min, as shown in Fig. S5. The color of the pellet changes slightly with the coverage, suggesting that there are some residual phases related to the CA surfactant (Fig. S5). For the kinetic study, in situ densification was performed using a press equipped with a dilatometer (Fig. S1). The densification behavior is divided into four zones, as shown in Fig. 4(a). In zone 1, densification is mostly related to particle rearrangement. Between 45 and 85 °C, an increased rate in particle rearrangement is observed. It may also be linked with the partial dehydration of the Ba (OH)2·8H2O transient phase, and that could enable hydroxyls to activate the mobility of CA on the surface, as was previously reported on TiO₂. 43,44 It is in zone 2 that most of the mechanochemical effects in cold sintering begin. The densification curves of all the samples look almost superimposed, which would imply a nearly similar densification rate and hence force–flux relationship 6,45 in the early moments of pressure solution. To thoroughly analyze densification in this zone, the axial strain rate $(\dot{\varepsilon})$ in this time interval was determined using Eq. (6), as proposed by Hellman *et al.*, 6

$$\dot{\varepsilon} = \frac{\partial l/\partial t}{l},\tag{6}$$

where $\partial l/\partial t$ is the time derivative of the axial strain ε , normalized to the instantaneous length of the sample l. The axial strain (ε) is defined as $\varepsilon=(l_0-l)/l_0$, with l_0 being the original length of the sample.

The strain rate $(\dot{\varepsilon})$ of different samples in zone 2 [Fig. 4(c)] decreases systematically with the amount of CA coverage but highlights a small variance in this zone. Since dissolution is enhanced at the beginning in the pressure solution, this implies that the stress-induced dissolution at the grain-to-grain contact is only very slightly perturbed by the presence of the adsorbed CA. In zone 3 (between 450 and 1200 s and isothermal region), there is a significant divergence in the evolution of time-dependent densification between all the samples [Fig. 4(a)]. A more detailed analysis in this zone shows that the strain rate $(\dot{\varepsilon})$ decreases with the CA coverage [Fig. 4(d)], but the most significant change in $\dot{\varepsilon}$ is related to the addition of surfactants in the system. With this observation, we can assume that the presence of surfactants affects diffusion and/or precipitation kinetics. Zone 4 is related to the last step of sintering under our processing conditions. After the dwell time of 75 min, the final relative densities are 95.0%, 94.7%, 94.3%, and 93.5% for samples with 0, 0.25, 1, and 2CA coverage, respectively [Fig. 4(b)]. As high relative densities are achieved, one can assume that adsorbed CA mainly acts as a barrier, slowing down the diffusion and/or precipitation kinetics in cold sintering. In spite of consistent trends and values, small discrepancies are observed between the relative densities in Fig. S5 and Fig. 4(b). They are due to the use of another die system designed for the in situ densification investigation and the use of a straight heating ramp from room temperature to 200 °C.

The SEM images of the microstructure after the cold sintering process for the different CA coverages are shown in Figs. 5(a)-5(f). All these densified materials have relative densities ranging between 92% and 96%. A dense microstructure is obtained for BT-0CA [Fig. 5(a)], while a small population of pores can be observed in the microstructures of ceramics obtained with CA-functionalized BaTiO₃ powders. The average grain size, of approximatively 100 ± 30 nm, was not significantly impacted by the CA coverage. These observations are in good agreement with microstructures obtained by low magnification TEM images for samples BT-0CA [Fig. 5(g)] and BT-4CA [Fig. 5(j)]. On the one hand, Fig. 5(h) shows a representative triple point for the BT-0CA sample (from bare BaTiO₃), which confirms low surface energy in the system as triple junctions are near equilibrium (with angles of $\sim\!120^\circ).^{46,47}$ On the other hand, for the BT-4CA sample (from CA-covered BaTiO₃), the microstructure shows triple junctions in some cases and four-grain junctions in other cases, especially near open pores. A further example of this with marked-up junctions of triple points, and high number of coordinated grain junctions, is found in Fig. S6. The EDS efforts did

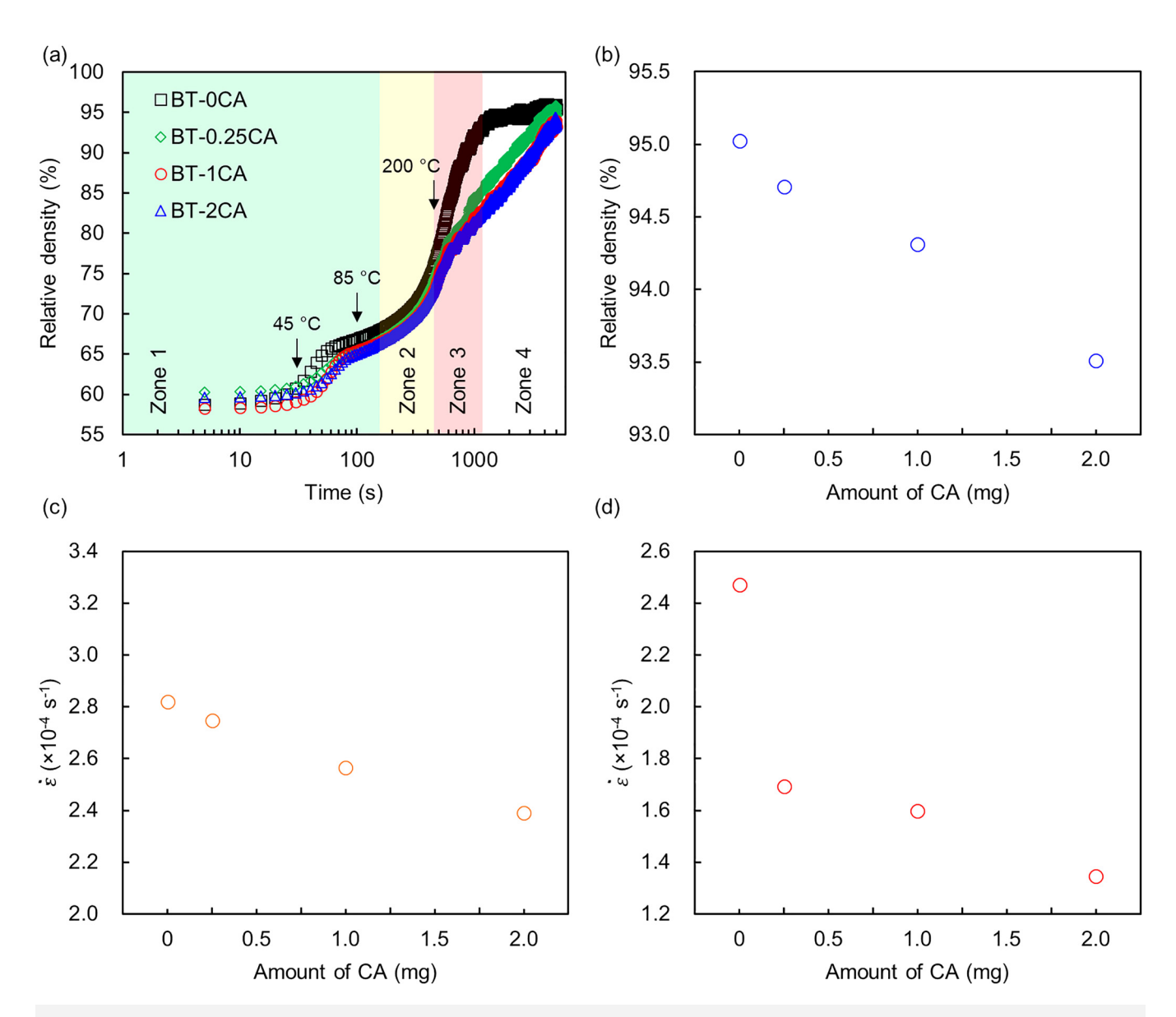


FIG. 4. (a) Time-dependent evolution of the relative density of BaTiO₃ with different CA coverages. Influence of adsorbed CA on the (b) relative density and the strain rate (\$\deccep\$) in (c) zone 2 and (d) zone 3.

not reveal the carbon phase clearly, so we suspect that the thinning process preferentially removed these phases. However, BaTiO₃ nanoparticles with approximatively 5 nm sometimes precipitate in triple points, as observed in Fig. 5(k). Such precipitation is possible; as we have reported on before, the solute typically precipitates epitaxially on pore surfaces. However, as nucleation is usually regarded as limited in confined volumes, the surfactant environments may help to overcome the issues associated with confinement.⁴⁸ Also, as previously shown in Fig. 4, the presence of CA does not significantly affect that step that is rate-dominated by dissolution [zone 2, Fig. 4(c)], but does

significantly affect the step that is rate-dominated by diffusion and precipitation [zone 3, Fig. 4(d)]. This may result in the supersaturation of the transient fluid, subsequently leading to the formation of an important number of BaTiO₃ nuclei and following nanoparticles, thanks to the stabilization by the surfactant, as shown in Fig. 5(k). Furthermore, He *et al.* reported that a slight supersaturation in the fluid phase could prevent the diffusion along grain boundaries during pressure solution creeps. ⁴⁹ This observation may provide an additional insight on the mass transport kinetics decrease in the presence of surfactants during cold sintering. Another important

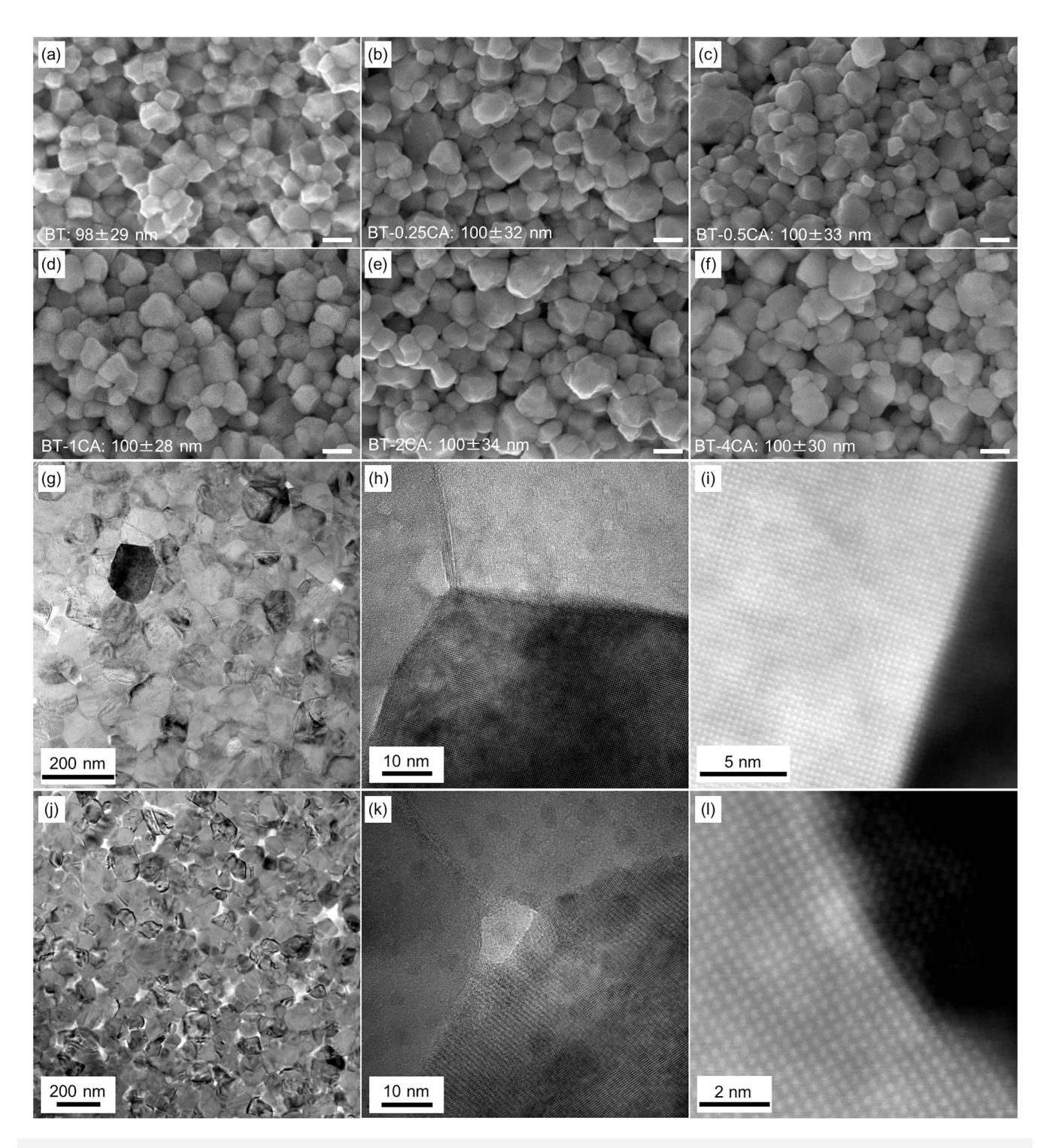


FIG. 5. SEM images of cold sintered BaTiO₃ with different CA coverages. (a) 0, (b) 0.25, (c) 0.5, (d) 1.0, (e) 2.0, and (f) 4.0 mg of CA were mixed with BaTiO₃ powders and named as BT, BT-0.25CA, BT-0.5CA, BT-1CA, BT-2CA, and BT-4CA, respectively. The grain size after cold sintering was shown in each image. Scale bar: 100 nm. TEM images of BaTiO₃ with [(g)-(i)] 0 and [(i)-(i)] 4 CA coverage. [(g) and (i)] Low magnification images and high magnification images of [(h)] and [(h)] triple points and [(h)] grain boundaries.

observation in the TEM study is the roughness of the grain boundary with a terrace ledge kink, as shown in Fig. 5(1).⁵⁰ Compared to the grain boundary of BaTiO₃ without CA [Fig. 5(i)], this type of structure was often observed in the sample with CA. Although dynamic stability of interface roughness is still subjected to debate, oroughness at interfaces can prevail following the effects of heterogeneous dissolution induced by the presence of defects or impurities (addition of CA in our case), or when there is a discontinuous fluid phase at local contact points between grains during dissolution. S2,53

Temperature dependent dielectric properties of the samples after the cold sintering process for the different CA coverages are shown in Figs. S7(a)-S7(b). There is a broadened and decreased maximum permittivity around 125 °C with CA increased coverage. In addition, the Curie-maximum temperature (Tm) decreases slightly with the increased coverage [Fig. S7(c)]. It could be due to the small nanoparticles, as we observed at the triple point with TEM. The decrease in the permittivity is a much bigger effect than can be accounted for from the porosities [Fig. S7(d)] and the volume fraction of CA [Fig. S7(e)]. The trend is different from the effect of polymer on the permittivity trend of cold sintered BaTiO₃-polymer composite, where it is well described with the mixing law.⁵⁴ Given that the chemisorbed CA on BaTiO₃ hinders the epitaxial reprecipitation, the dead layer (nonferroelectric layer) on BaTiO3 might be increased as a result of the disturbed precipitation. On the other hand, resistivity increases by an order of magnitude with an increased coverage and reaches $\sim 10^{12} \Omega$ cm for the BT-4CA [Fig. S7(f)]. This implies that, although we did not observe the carbon phase by TEM-EDS, there are residual CA at the grain boundaries after cold sintering. Furthermore, the thorough analysis of FTIR spectra in different samples lets us assume that the chemical integrity of the CA surfactant is preserved after cold sintering (Fig. S4).

In summary of all the above experimental observations related to CA surfactant coverage in cold sintering BaTiO₃:

(1) Final relative density decreases (96%–92% TD) systematically with increased coverage.

- (2) Precipitation rates that drive the closing of the pore shrinkage, as determined from densification rates at higher densities, decrease with increasing coverage.
- (3) Final average grain size is not impacted by the coverage.
- (4) Grain boundary roughness is enhanced with coverage.
- (5) Microstructure is spatially demonstrating regions of different levels of stages of pore closure with coverage.
- (6) Resistivity increases by an order of magnitude with increased coverage, consistent with the CA surfactant coverage in the grain boundaries.
- (7) The decrease in relative permittivity with CA increased coverage is a much bigger effect than can be accounted for from the porosities and the volume fraction of CA.

From the above observations, we make the following hypothesis on the dynamics impacting the cold sintering stages. We propose this mechanism guided by the data presented above and other studies in the literature. 44,55

Figure 6 contrasts the surface with non-coverage [Fig. 6(a)] and with coverage [Fig. 6(b)] of the surfactant. The typical cold sintering process is noted with Fig. 6(a) and is involving the pressure solution creep process that drives dissolution and precipitation, the diffusional fluxes being set up with the local stress and associated chemical potential gradients. This process is still active with the coverage of surfactants, but now the kinetics have to be considered with respect to the surfactants, and the schematic reflects the experimental observations listed above. The surfactants are considered with a coverage on both adjacent grains. As these surfaces come together, the two monolayers interact and drive migration of the surfactant molecules out of the grain boundary region into the pore junctions; the hydroxyls on the surface can aid this process, along with the stress gradients.⁴⁴ As cold sintering proceeds, the dissolution in the contact regions is favored to the interface and the regions without CA surfactants; this creates an etching effect and thereby terraces and kinks. The kinks themselves may be sites for preferential CA site occupancy, as noted with atomic force microscopy (AFM), and

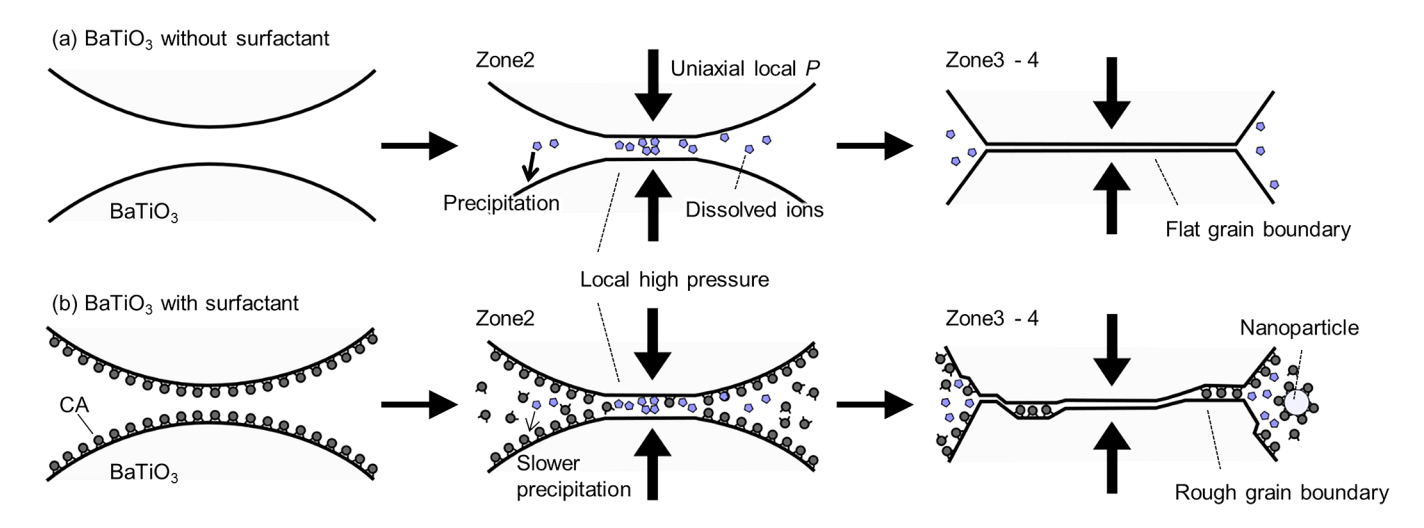


FIG. 6. Hypothesis on the dynamics impacting the cold sintering stages (a) without and (b) with CA surfactants.

leave a partial residual surfactant in the grain boundary.⁵⁵ The solute from the dissolution will diffuse to the pore regions and/or other areas of lower chemical potential. There is excessive surfactant transport under the local stress gradients and accumulation in lowpressure regions. The BaTiO₃ solute species will also be transported away from the high-stress regions and will precipitate preferentially on regions that are not covered with surfactants. With the surfactant on the surface, the sintering process will be kinetically slowed down, create a roughness between the boundaries, and leave a higher residual porosity. This is what we observed in the densification data and also in the TEM observations. In some of the triple point pores, we also noted in TEM studies that there can be the precipitation of nano-BaTiO₃ that are ~ 5 nm [Fig. 5(k)]. The increase in the resistivity implies that there is still a residual monolayer of surfactants in the grain boundaries, but most of the surfactants are now transported to the pore (low-pressure) regions and limit the final stages of densification. We note that resistivity increases by an order of magnitude in the case of the higher coverage powders; this could be due to the residual surfactants and also the roughness and defects in these interfaces. These interfacial regions are lowering the dielectric constant of densified BaTiO3 with increasing the surfactant coverage on the powders. The decrease in dielectric constant is much greater than the changes in porosity and volume fraction of CA, as predicted by the Rushman-Strivens model [(Eq. (S1)] and the mixing law [(Eq. (S3)]. This points to a layer at the grain boundaries that is not a complete monolayer but is still improving the resistivity in the final densified ceramics.

IV. CONCLUSIONS

Both surfactant coverage and sintering are processes that reduce the excessive surface energy. Here, BaTiO₃ particles are grafted with different coverages with a catechol (CA) surfactant, and then these particles are densified under cold sintering. The degree of CA adsorption is determined experimentally and quantified with the Langmuir adsorption isothermal model. The data fit extremely well and are consistent with an isothermal adsorption process; it determines the equilibrium adsorption coefficient, K, and the maximized coverage or grafting density, θ_{∞} , for saturated monolayer coverage. A Ba(OH)₂·8H₂O transient phase is used to enable low-temperature densification, so there is then a competition between the surfactant coverage and the processes that drive the cold sintering process. Dilatometry quantifies densification and considers a major part of the densification in different zones, linked to dissolution, and precipitation. Microstructure is observed with TEM to determine the grain and grain boundary interfaces that result with the competition of surfactant coverage and densification driven by the dissolution and reprecipitation processes at the interfaces. A mechanism with the redistribution of surfactants in the interfaces and retardation of the cold sintering kinetics is discussed, based on these experimental observations, with the major impact on the diffusion and/or precipitation kinetics limiting the residual porosity removal as a function of surfactant coverage. We here introduce the unusual situation of a competition between surfactant coverage and sintering. The mixing of such phenomena has been previously not considered because the typical sintering temperatures are so high that surfactants would be decomposed on heating to the sintering temperatures, which are

normally $\sim 1000^{\circ}$ C. With cold sintering, the densification mechanism occurs with a surfactant still chemically stable in the system. The above paper objective is to consider the basic processes and impact of such a competition; we do not regard this as the first efforts to design grain boundary interfaces with such surfactants, and the details of the mechanisms need major levels of investigation to gain understanding of the cold sintering process, and also the optimal design of interfaces enabled with surfactants.

SUPPLEMENTARY MATERIAL

See the supplementary material for the dilatometer apparatus for the $in\ situ$ densification investigation, SEM images of powders before and after CA treatment, UV–vis absorption data, FTIR, relative density of cold sintered BaTiO $_3$ with the different grafting density, low magnification TEM bright-field image, and electrical properties of cold sintered BaTiO $_3$ with and without CA coverages.

ACKNOWLEDGMENTS

T.S. would like to acknowledge the Kyocera Corporation for funding his fellowship, enabling his time as a visiting scientist at the Penn State University. A.N., Z.F., and C.A.R. were partially supported by the AFOSR grant (Grant No. FA9550-19-1-0372). C.A.R. was supported by the U.S. National Science Foundation (NSF) (No. DMR-1728634). We also wish to thank the staff of the MCL for aid in sample preparation and in maintaining electrical measurement facilities. We also thank Joanne Aller for helping in proofreading and formatting this publication.

DATA AVAILABILITY

The data that support the findings of this study are available from the corresponding author upon reasonable request.

REFERENCES

¹M. N. Rahaman, Ceramic Processing and Sintering (Talyor and Francis Group, 2003).

²S. Grasso, M. Biesuz, L. Zoli, G. Taveri, A. I. Duff, D. Ke, A. Jiang, and M. J. Reece, Adv. Appl. Ceram. 119, 115 (2020).

³J. Guo, H. Guo, A. L. Baker, M. T. Lanagan, E. R. Kupp, G. L. Messing, and C. A. Randall, Angew. Chem. Int. Ed. 55, 11457 (2016).

⁴M. F. Ashby, "A first report on sintering diagrams," Acta Metall. 22, 275–289

⁵A. Ndayishimiye, M. Y. Sengul, T. Sada, S. Dursun, S. H. Bang, Z. A. Grady, K. Tsuji, S. Funahashi, A. C. T. van Duin, and C. A. Randall, Open Ceram. 2, 100019 (2020).

⁶R. Hellmann, J. P. Gratier, and R. Guiguet, in *Water-Rock Interactions, Ore Deposits, and Environmental Geochemistry. A Tribute to David A. Crerar* (The Geochemical Society, Special Publication, 2002), pp. 129–152.

⁷P. K. Weyl, J. Geophys. Res. **64**, 2001, https://doi.org/10.1029/JZ064i011p02001 (1959).

⁸X. Zhang and C. J. Spiers, Geochim. Cosmochim. Acta 69, 5681 (2005).

⁹D. W. Durney, Nature **235**, 315 (1972).

¹⁰D. Vollath, F. D. Fischer, and D. Holec, Beilstein J. Nanotechnol. 9, 2265 (2018).

11 C.-Y. Hui and A. Jagota, Langmuir 29, 11310 (2013).

¹²J. N. Israelachvili, *Intermolecular and Surface Forces* (Academic Press, 1991).

¹³K. Tsujii, Surface Activity: Principles, Phenomena and Applications (Academic Press, 1998).

- ¹⁴H. Zhang and J. F. Banfield, Chem. Mater. 17, 3421 (2005).
- ¹⁵L. Zeininger, L. Portilla, M. Halik, and A. Hirsch, Chem. Eur. J. 22, 13506 (2016).
- ¹⁶M. B. McBride and L. G. Wesselink, Environ. Sci. Technol. 22, 703 (1988).
- ¹⁷M. K. Abugazleh, B. Rougeau, and H. Ali, J. Environ. Chem. Eng. 8, 104180 (2020).
- ¹⁸M. D. Clark, J. Nanoparticle Res. **16**, 2264 (2014).
- ¹⁹T. R. Bastami, M. H. Entezari, Q. H. Hu, S. B. Hartono, and S. Z. Qiao, Chem. Eng. J. 210, 157 (2012).
- ²⁰A. Ratkovich and R. L. Penn, Mater. Res. Bull. 44, 993 (2009).
- ²¹N. Sakurai, V. Bojan, J. J. Stapleton, G.-Y. Yang, C. A. Randall, Y. Mizuno, and H. Chazono, Jpn. J. Appl. Phys. 48, 61404 (2009).
- ²²R. Floyd, S. Lowum, and J.-P. Maria, Rev. Sci. Instrum. **90**, 055104 (2019).
- ²³U. Terranova and D. R. Bowler, J. Phys. Chem. C 114, 6491 (2010).
- ²⁴S.-C. Li, J. Wang, P. Jacobson, X.-Q. Gong, A. Selloni, and U. Diebold, J. Am. Chem. Soc. 131, 980 (2009).
- ²⁵S. Bahri, C. M. Jonsson, C. L. Jonsson, D. Azzolini, D. A. Sverjensky, and R. M. Hazen, Environ. Sci. Technol. 45, 3959 (2011).
- 26F. Sallem, L. Villatte, P.-M. Geffroy, G. Goglio, and C. Pagnoux, Colloids Surfaces A Physicochem. Eng. Asp. 602, 125167 (2020).
- ²⁷R. Rodríguez, M. A. Blesa, and A. E. Regazzoni, J. Colloid Interface Sci. 177, 122 (1996).
- ²⁸T. D. Savić, I. A. Janković, Z. V. Šaponjić, M. I. Čomor, D. Ž. Veljković, S. D. Zarić, and J. M. Nedeljković, Nanoscale 4, 1612 (2012).
- ²⁹T. Eda, J. Fujisawa, and M. Hanaya, J. Phys. Chem. C 122, 16216 (2018).
- ³⁰J. Fujisawa, T. Eda, and M. Hanaya, J. Phys. Chem. C **120**, 21162 (2016).
- ³¹J. T. Davies and E. K. Rideal, *Interfacial Phenomena*, 2nd ed. (Academic Press, New York, 1963).
- 32R. H. French, J. Am. Ceram. Soc. 83, 2117 (2000).
- ³³R. H. French, V. A. Parsegian, R. Podgornik, R. F. Rajter, A. Jagota, J. Luo, D. Asthagiri, M. K. Chaudhury, Y. Chiang, S. Granick, S. Kalinin, M. Kardar, R. Kjellander, D. C. Langreth, J. Lewis, S. Lustig, D. Wesolowski, J. S. Wettlaufer, W.-Y. Ching, M. Finnis, F. Houlihan, O. A. von Lilienfeld, C. J. van Oss, and T. Zemb, Rev. Mod. Phys. 82, 1887 (2010).
- 34R. H. R. Castro and D. Gouvêa, J. Am. Ceram. Soc. 99, 1105 (2016).
- ³⁵G. Goglio, A. Ndayishimiye, A. Largeteau, and C. Elissalde, Scr. Mater. 158, 146 (2019).

- ³⁶A. Ndayishimiye, A. Largeteau, S. Mornet, M. Duttine, M.-A. Dourges, D. Denux, M. Verdier, M. Gouné, T. Hérisson de Beauvoir, C. Elissalde, and G. Goglio, J. Eur. Ceram. Soc. 38, 1860 (2018).
- ³⁷S. H. Bang, A. Ndayishimiye, and C. A. Randall, J. Mater. Chem. C 8, 5668 (2020).
- ³⁸J. Guo, X. Zhao, T. Herisson De Beauvoir, J.-H. Seo, S. S. Berbano, A. L. Baker, C. Azina, and C. A. Randall, Adv. Funct. Mater. 28, 1801724 (2018).
- ³⁹T. Sada, Z. Fan, A. Ndayishimiye, K. Tsuji, S. H. Bang, Y. Fujioka, and C. A. Randall, J. Am. Geram. Soc. **104**, 084103 (2020).
- ⁴⁰A. J. Allen, I. Levin, R. A. Maier, S. E. Witt, F. Zhang, and I. Kuzmenko, J. Am. Ceram. Soc. **104**, 2442 (2021).
- ⁴¹M. Y. Sengul, J. Guo, C. A. Randall, and A. C. T. van Duin, Angew. Chem. Int. Ed. 58, 12420 (2019).
- ⁴²A. Ndayishimiye, M. Y. Sengul, D. Akbarian, Z. Fan, K. Tsuji, S. H. Bang, A. C. T. van Duin, and C. A. Randall, Nano Lett. (2021).
- ⁴³T. Sada, K. Tsuji, A. Ndayishimiye, Z. Fan, Y. Fujioka, and C. A. Randall, J. Eur. Ceram. Soc. 41, 409–417 (2020).
- 44S.-C. Li, L.-N. Chu, X.-Q. Gong, and U. Diebold, Science 328, 882 (2010).
- **45**F. K. Lehner, Tectonophysics **245**, 153 (1995).
- 46G. Gottstein, Y. Ma, and L. S. Shvindlerman, Acta Mater. 53, 1535 (2005).
- 47 R. A. Marks and A. M. Glaeser, Acta Mater. 60, 349 (2012).
- ⁴⁸F. C. Meldrum and C. O'Shaughnessy, Adv. Mater. **32**, 2001068 (2020).
- ⁴⁹W. He, D. Sparks, and A. Hajash, J. Geophys. Res. Solid Earth 118, 497, https://doi.org/10.1002/jgrb.50064 (2013).
- 50 J. J. De Yoreo, L. A. Zepeda-Ruiz, R. W. Friddle, S. R. Qiu, L. E. Wasylenki, A. A. Chernov, G. H. Gilmer, and P. M. Dove, Cryst. Growth Des. 9, 5135 (2009).
- (2009).

 51 C. J. Spiers and P. M. T. M. Schutjens, Oil Gas Sci. Technol. Rev. IFP 54, 729 (1999).
- $\bf 52$ J.-P. Gratier, D. K. Dysthe, and F. Renard, in Advances in Geophysics (Elsevier, 2013), Vol. 54, pp. 47–179.
- ⁵³R. Raj, J. Geophys. Res. Solid Earth 87, 4731, http://doi.org/10.1029/ JB087iB06p04731 (1982).
- ⁵⁴T. Sada, K. Tsuji, A. Ndayishimiye, Z. Fan, Y. Fujioka, and C. A. Randall, J. Appl. Phys. **128**, 084103 (2020).
- 55L.-M. Liu, S.-C. Li, H. Cheng, U. Diebold, and A. Selloni, J. Am. Chem. Soc. 133, 7816 (2011).